



# Coastal Langmuir circulations induce phase-locked modulation of bathymetric stress

Kalyan Shrestha<sup>1</sup> · William Anderson<sup>2</sup> 

Received: 19 July 2019 / Accepted: 28 November 2019 / Published online: 7 December 2019  
© Springer Nature B.V. 2019

## Abstract

The ocean boundary layer (OBL) is forced by atmosphere-ocean and sea ice-ocean momentum fluxes, wave dynamics, and buoyancy; in coastal zones, OBL dynamics are further complicated by additional shear from the seafloor. Among numerous other phenomena, coastal mixing affects dispersion of anthropogenic quantities, erosion and turbidity, and benthic sequestration. In the OBL, interaction of wind-induced shear and surface waves manifests so-called Langmuir turbulence and distinctive Langmuir cells under favorable conditions, which have implications for the aforementioned coastal processes. Large-eddy simulation was used to dynamically sample the flow during relative extremes in bathymetric stress and vertical velocity. Probability density functions of vertical velocity are bimodal, the signature of persistent upwelling and downwelling within Langmuir cells, and this attribute manifests itself in the bathymetric stress, revealing a phase-locked modulation. We report modulation between negative vertical velocity (downwelling) and relatively elevated bathymetric stresses, thereby revealing that coastal Langmuir turbulence has direct implications for erosion and turbidity.

**Keywords** Langmuir circulations · Bottom-bed stress map · Bimodal probability distribution function

## 1 Introduction

The ocean boundary layer (OBL) occupies the upper  $\approx 100$  m of Earth's oceans, and is forced by atmosphere-ocean and sea ice-ocean momentum fluxes, wave dynamics, and buoyancy. In coastal zones, OBL processes are further influenced by bottom-boundary layer shearing, which affects column mixing and aggregate transport processes. Among a host of other phenomena, coastal OBL dynamics affect advective dispersion of anthropogenic quantities—including those associated with hypoxic conditions; in addition, and as explored herein, coastal OBL dynamics impact erosion and turbidity.

---

✉ William Anderson  
william.anderson@utdallas.edu

<sup>1</sup> School of Oceanography, The University of Washington, Seattle, WA 98195, USA

<sup>2</sup> Mechanical Engineering Department, The University of Texas at Dallas, Richardson, TX 75080, USA



Under favorable conditions, interaction of wind-induced shear and surface waves manifests Langmuir turbulence and the distinctive Langmuir cells in the coastal OBL [1–6]. Inspection of the vorticity transport equations reveal that the simultaneous presence of Stokes drift (aggregate drift due to surface waves) and imposed aerodynamic surface stresses enables a tilting of ambient vertical vorticity into the streamwise direction, providing sustenance for quasi-streamwise Langmuir cells [7–10]. In this manuscript, the first, second, and third component of any vector corresponds with its scalar magnitude in the streamwise, spanwise, and vertical direction, respectively, where the streamwise direction has been aligned with the primary transport direction throughout. A relatively larger prior research effort has been devoted to Langmuir turbulence in open-ocean conditions ([11, 12] and references therein). However, Langmuir turbulence and OBL processes in coastal zones are also of pivotal importance to coastal biodiversity, turbidity, etc. [13–15].

In coastal zones, OBL processes are complicated by resultant bathymetric hydrodynamic stresses. In a numerical sense, this scenario is realized by a non-zero Stokes drift velocity at the seafloor, thereby guaranteeing that the aforementioned streamwise vorticity sustenance arguments are influenced by the bounding presence of the seafloor. In such scenarios, Langmuir circulations occupy the depth of the water column and significantly alter turbulence characteristics near the bottom-wall region [14–19]. Coastal-zone Langmuir cells are strongly coherent and full depth [13–17, 19–24], which means that the transient, counter-rotating cells not only have patterns of surface convergence and divergence [25–28] known as “windrows”, but also impose phase-locked modulation of the bathymetric surface stresses. In spite of the distinct physical importance of this, to our knowledge no preceding study has specifically provided evidence and/or quantification of the resultant bed stress due to Langmuir cells. For this study, we have used large-eddy simulation (LES) of coastal-zone OBL processes to highlight the interconnected nature of Langmuir turbulence and bathymetric stress. For the coastal-zone OBL, the so-called roughness Reynolds number provides a means to assess the flow inertial conditions in a bulk sense,  $Re_H = u_* H \nu_w^{-1}$ , where  $u_*$  is the bathymetric friction velocity,  $H$  is the column depth, and  $\nu_w$  is the kinematic viscosity. For the settings considered herein, preliminary analysis reveals that  $Re_H \sim \mathcal{O}(10^6)$ , which qualifies the flow as inertia dominated, or fully rough, and, as such, the present wall-modeled LES approach is the only suitable numerical tool for studying the flow. Others have used DNS to model coastal-zone OBL dynamics, but at far lower  $Re_H$  [18], while yet others have looked specifically at surface stress variability for canonical flows, but for cases with  $Re_H \sim \mathcal{O}(10^3)$  [29]. At these relatively lower values of  $Re_H$ , the autonomous inner cycle is preserved within the flow and dynamics of this cycle influence surface stress; however, for the  $Re_H$  values typical of the coastal OBL, this inner cycle is ablated by turbulence and wall-modeled LES is the only plausible approach to numerical investigation. We note, however, that numerous studies have shown that wall-modeled LES under inertia-dominated conditions can be used to recover surface stress [30].

Description of the problem under consideration—which is designed to replicate natural conditions realized in the field—along with the governing equations and numerical techniques, are presented in Sect. 2. This is followed by a series of results derived from flow processing and accompanying discussions in Sect. 3. Concluding remarks are presented in Sect. 4.



## 2 Problem formulation

### 2.1 Governing equations

The grid-pass filtered (i.e., LES), wave-averaged non-dimensional Craik–Leibovich (CL) equations are written as:

$$\frac{\partial \tilde{\mathbf{u}}}{\partial t} + \frac{1}{2} \nabla (\tilde{\mathbf{u}} \cdot \tilde{\mathbf{u}}) - \tilde{\mathbf{u}} \times \tilde{\boldsymbol{\omega}} = -\nabla \tilde{\pi} - \nabla \cdot \boldsymbol{\tau} + \frac{1}{La_t^2} (\mathbf{u}_s \times \tilde{\boldsymbol{\omega}}), \quad \text{and} \quad \nabla \cdot \tilde{\mathbf{u}} = 0, \quad (1)$$

where  $\tilde{\dots}$  denotes a grid-filtered quantity,  $\tilde{\pi} = \tilde{p}/\rho + \frac{1}{2} [|\tilde{\mathbf{u}} + \mathbf{u}_s|^2 - |\tilde{\mathbf{u}}|^2]$  is the generalized dynamic pressure, and  $\boldsymbol{\tau} = \mathbf{u}' \otimes \mathbf{u}' - \tilde{\mathbf{u}}' \otimes \tilde{\mathbf{u}}'$  is the subgrid-scale stress tensor, where superscript prime denotes fluctuation from the Reynolds average. Here, the viscous stress tensor is omitted owing to the very high Reynolds number conditions typical of the OBL.  $La_t^{-2}(\mathbf{u}_s \times \tilde{\boldsymbol{\omega}})$  is a vortex force that sustains Langmuir circulations, where  $La_t = (u_w/U_s)^{1/2}$  is the turbulent Langmuir number,  $\mathbf{u}_s$  is the Stokes drift profile (discussion to follow), and  $\tilde{\boldsymbol{\omega}} = \nabla \times \tilde{\mathbf{u}}$  is ambient vorticity in the column [11]; in the definition of  $La_t$ ,  $u_w = (\tau_a^w/\rho_a)$  is the shear velocity associated with aerodynamic drag from the atmospheric surface layer, and  $U_s$  is the magnitude of the surface Stokes drift profile.  $\mathbf{u}_s$  represents the aggregate wave orbital drift and incorporates the sole effect of surface waves and thus the wave-averaged sea surface is assumed flat. The CL equations shown in Eq. 1 are standard for open-ocean conditions [11], where there is no additional shear due to bathymetric drag.

However, Langmuir cells in coastal regimes differ from open ocean regimes due to the presence of bottom boundary layer shear [31], which generates an additional shear velocity for the bathymetric stress,  $u_*$ . It can be immediately deduced, then, that  $La_t$  does not encompass all relevant forces, and instead new parameters,  $\psi_1$  and  $\psi_2$ , are defined to fully capture the range of independent problem parameters [17, 32, 33]:

$$\psi_1 = \frac{u_w}{u_*} \quad \text{and} \quad \psi_2 = \frac{U_s}{u_*}, \quad (2)$$

where  $u_*$  represents bottom-wall friction velocity. It is noted that in the present study, the wind and waves are co-aligned in the streamwise direction and the surface wave field is monochromatic; these conditions help to narrow the complexity of the problem, without undermining key scientific deductions derived from the research effort. The Stokes drift velocity profile in coastal regimes can be defined as [15]:

$$\mathbf{u}_s = \phi_s \hat{i} + 0 \hat{j} + 0 \hat{k}, \quad \text{where} \quad \phi_s = U_s \frac{\cosh[2k(z+H)]}{2 \sinh^2[kH]}, \quad (3)$$

where,  $z = H$  is the average surface height,  $H$  is the water column depth, and  $k$  is the dominant wavenumber of the surface waves. In this study, further assumptions based on prior field observations [13, 14] and numerical studies of coastal Langmuir turbulence [15, 17, 20] are made. Coriolis accelerations are eliminated, owing to the high Rossby number conditions of coastal-zone OBL eddies, and vertical buoyancy fluxes are neglected on the presumption that OBL processes homogenize the column in coastal zones. Also, Gargett and Wells [14] have reported that Langmuir forcing was dominant over buoyancy forcing for “Record 43.025” (details to follow in the next section), the coastal case under consideration in this numerical study. Having adopted this alternative problem formulation for coastal zones, the vortex forcing term in Eq. 1 becomes  $\psi_2(\mathbf{u}_s \times \tilde{\boldsymbol{\omega}})$ . This is attained upon



normalization of Eq. 1 by the bottom friction velocity,  $u_*$  that accounts for the affect of benthic stresses relevant to coastal regimes, instead of surface friction velocity,  $u_w$ , used in the conventional normalization procedure for open-ocean scenarios (please see Shrestha et al. [19]). As such, the vortex force prefactor,  $La_t^{-2}$ , gets replaced by  $\psi_2$  in the vortex forcing term in Eq. 1.

## 2.2 Posing the coastal Langmuir turbulence problem

In order to provide context for the results, we have used LES to model cases closely resembling “Record 43.025” from the field observations at the shallow shelf coastal region of New Jersey ( $H = 15$  m water-column depth) [14]. The recorded intermediate waves are characterized by amplitude,  $a = 0.7$  m, frequency,  $f_w = (gk \tanh kH)^{1/2} = 0.82$  rad/s, and wavenumber,  $k = 2\pi/\Lambda = 0.08$  rad/m, corresponding to wavelength,  $\Lambda = 79$  m. With the given wave characteristics, surface velocity of a constant, streamwise-aligned, monochromatic Stokes drift profile given by Eq. 3 can be calculated as  $U_s = f_w ka^2 \coth kH = 0.038$  m/s. Similarly, a constant wind stress is assumed at the top surface with value,  $\langle \tau_{xz,a}^w \rangle_{xyt} = 0.079$  N/m<sup>2</sup>, corresponding to surface friction velocity  $u_w = 0.28$  m/s; in this document, averaging over dimension,  $a$ , is denoted with  $\langle \dots \rangle_a$ . Now, to allow the ratio  $\psi_1 = 1$  (Eq. 2), it follows that the bottom bed stress is  $\langle \tau_{xz,w}^w \rangle_{xyt} = \rho_w u_*^2 = \rho_w \psi_1 u_w^2 \approx 79$  N/m<sup>2</sup>; note that for this specific choice,  $\psi_1 \rightarrow La_t^{-2}$ , but we nevertheless preserve with inclusion of  $\psi_1$  given the need for generality in coastal conditions. In this study, we use  $\psi_1 = 1$  for practical convenience, since our interest here is phase-locked modulation and not the role of  $\psi_1$ . Numerous other groups have used this choice in complementary prior studies [16, 21, 28, 34], and we note a recent article that studies the influence of  $\psi_1$  under carefully-controlled conditions [19]. Furthermore, all these physically-motivated wind and wave parameters can be translated into relevant non-dimensional parameters:  $\psi_2 = 4.34$  (Eq. 2), turbulent Langmuir number,  $La_t = 0.48$ , depth-normalized wavenumber,  $kH = 1.2$ , and depth-normalized wavelength,  $\Lambda/H = 5.26$ .

Numerical integration of the Craik–Leibovich equations subjected to the described wind and wave forces is performed within a computational domain (transect shown in Fig. 1a), which is a rectangular prism with the dimensions:  $L_x = L_y = 2\pi H$  where the depth  $L_z = H = 15$  m. We have performed LES of the same flow with resolutions,  $\{N_x, N_y, N_z\} = \{96, 96, 96\}$ ,  $\{128, 128, 128\}$ , and  $\{192, 192, 192\}$ ; this resolution results in spatial resolution,  $\{L_x/N_x, L_y/N_y, H/N_z\} = \{0.982 \text{ m}, 0.982 \text{ m}, 0.156 \text{ m}\}$ ,  $\{0.736 \text{ m}, 0.736 \text{ m}, 0.117 \text{ m}\}$ , and  $\{0.491 \text{ m}, 0.491 \text{ m}, 0.078 \text{ m}\}$ . The repetition of cases across resolution is used to demonstrate that scientific deductions are unaffected by numerical attributes of the study. A constant wind force is imposed at the top boundary, along with prescription of the non-penetration condition for vertical velocity,  $\tilde{w}(x, y, z/H = 1, t) = 0$ . The present numerical approach is based on wall-modeled LES [35], and thus a model for momentum fluxes (surface stress) at the lower wall is required, vis.  $\tau_{iz,w}^w(x, y, t)/\rho = C_m(z)\tilde{u}_i(x, y, z, t)U(x, y, z, t)$ , where the momentum flux transfer function is defined via the presumption of equilibrium conditions,  $C_m(z) = -[\kappa/\log(z/z_0)]^2$ , where  $\kappa$  is the von Kármán constant and  $z_0/H = 10^{-2}$  is a pre-defined local roughness length assuming negligible seafloor undulations;  $U(x, y, z, t) = (\tilde{u}(x, y, z, t)^2 + \tilde{v}(x, y, z, t)^2)^{1/2}$ , where  $(\cdot)$  denotes a second test-filtered quantity, and used here to minimize local extremes in stress while also capturing spatial undulations in the bathymetric stresses.

Logarithmic layer scaling will, in fact, be disrupted by the passage of Langmuir cells in low Reynolds number flows [16], but recovers at high Reynolds number as reported by



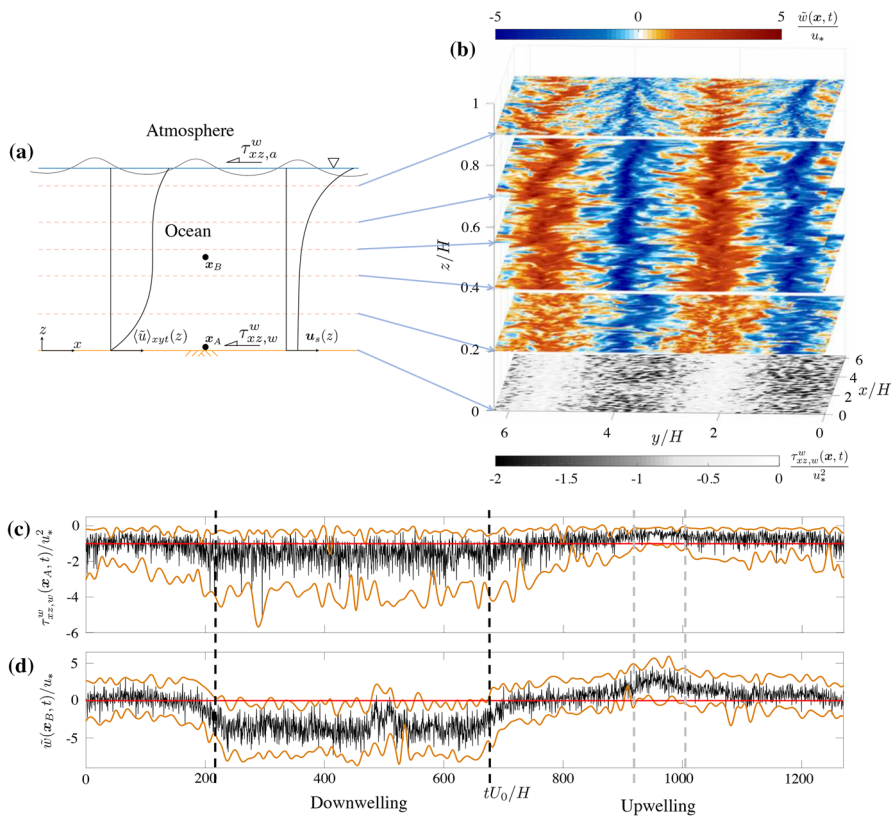


**Fig. 1** Panel **a** shows a streamwise–wall-normal transect of problem, with annotations for the Stokes drift profile,  $u_s(z)$ , and idealized streamwise velocity profile,  $\langle \tilde{u} \rangle_{xy}(z)$ . Panel **a** also includes annotations for imposed aerodynamic and hydrodynamic stresses,  $\tau_{xz,a}^w$  and  $\tau_{xz,w}^w$ , respectively, and discrete sampling locations,  $x_A = \{L_x/2, L_y/2, \Delta_z/2\}$  and  $x_B = \{L_x/2, L_y/2, H/2\}$ , where  $\Delta_z = L_z/N_z$  is the vertical computational mesh resolution, while  $\Delta_z/2$  is the first location at which stress is stored in the wall-modeled, staggered grid LES formulation used herein. From a simulation of the Panel **a** problem, Panel **b** shows horizontal planes of instantaneous vertical velocity at a series of vertical locations (blue-white-red color floods at  $z/H = 0.2, 0.4, 0.55, 0.7$ , and  $0.9$ ) and corresponding instantaneous hydrodynamic bathymetric stress (black-white color flood). Panels **c** and **d** show time-series evolution of  $\tau_{xz,w}^w(x_A, t)/u_s^2$  and  $\tilde{w}(x_B, t)/u_s$ , with annotations for periods of predominant “Downwelling” and “Upwelling” provided beneath Panel **d**. For perspective, the Reynolds-averaged quantity (solid red) and time-series envelope (solid orange) have been superimposed on Panels **c** and **d**

Deng et al. [18]. Use of this modeling approach does not assume that equilibrium conditions exist at all times everywhere in space—indeed, mixing in the flow induces instantaneous conditions that never agree with the time average. Rather, it is a matter of necessity that some form of surface stress closure is needed. It is emphasized that many years of research have supported this space-local implementation of the logarithmic law for surface stress (for example, see Bou-Zeid and company [36] or Anderson and company [37–39]). It has been shown that space-local version of stress enable realistic stress undulations. A very recent article from Shrestha and company [19] assessed dynamical response of coastal zone Langmuir turbulence to a range of forcing conditions (and forcing alignments).



The study also provided vertical profiles of plane- and phase-averaged constituent terms of the transport equation for turbulent kinetic energy, *tke*. The profiles comprehensively show that the vortex forcing term makes a modest contribution to the *tke* balance within the bottom-boundary layer, relative to shear production of subgrid-scale dissipation. This result is a basis for use of the present wall modeling approach. In the wall modeling closure approached described herein,  $\kappa$  and  $z_0$  are user-defined input arguments, and as such are independent parameters of the problem. A recent article has shown that  $\kappa$  can vary [18], while the roughness length varies based on geometric attributes of the seafloor; the prescribed  $z_0$  value is designed to capture ‘typical’ conditions. The focus of this study was assessment of phase-locked modulation of hydrodynamic stress, and it is beyond the scope of this study to perform parametric assessment of  $\kappa$  and  $z_0$ . Note that Reynolds number could be defined in a number of ways, where all would confirm that the flow is inertial dominated or “fully rough”, for example,  $Re_H = u_* H / \nu_w \sim \mathcal{O}(10^6)$ . We stress that the present flow solver has no capacity to resolve surface wave flow physics, and instead the influence of waves are parameterized via the orbital Stokes drift profile described in Sect. 2.1 (Eq. 3). This modeling approach is needed to regulate the problem complexity, but we emphasize once more that the results observed are a product of the user-defined numerical conditions. For reference, we direct readers interested in the influence of surface waves to Fredsoe and company [40, 41], who used experimental campaigns to measure bed stress in free-surface flows subjected to waves, pressure gradient, and superposition of these forces at a range of conditions. Although Langmuir cells were not present in these flows, Fredsoe and company [40, 41] nevertheless showed that waves influence bed stress, and as such future work with generalized Stokes drift profiles is needed; such work is beyond the scope of the present article. Spectral discretization is used in the horizontal direction, which imposes periodicity on the vertical “walls” of the computational domain. Spatial derivatives in the vertical direction are evaluated by the centered, second-order finite differencing scheme. Second-order Adam-Bashforth time integration is used to advance Equation 1. The nonlinear advective term is dealiased with the 3/2 rule in Fourier space [42]. The LES code is an extension of the John Hopkins University (JHU) LES code [36, 43] to simulate coastal Langmuir turbulence [17].

### 3 Results and discussion

#### 3.1 Phase-locked modulation of bathymetric stresses

Firstly, it is to be noted that the following analysis of results considers mature stage of Langmuir circulations, which means that the turbulence statistics obtained from the LES solutions of phase-averaged CL equations have become stationary. Figure 1b displays contours of instantaneous, resolved, vertical velocity,  $\tilde{w}(\mathbf{x}, t)/u_*$ , at different depths of the water-column ( $z/H = 0.2, 0.4, 0.55, 0.7, 0.9$ ), along with the associated instantaneous bathymetric stress map. Please note that  $z/H = 0$  and 1 correspond to the bottom and top of the water column, respectively. Firstly, the presence of strongly coherent, counter-rotating cells with alternating regions of upwelling ( $\tilde{w}(\mathbf{x}, t)/u_* > 0$ ) and downwelling ( $\tilde{w}(\mathbf{x}, t)/u_* < 0$ ) motions, colored by red and blue, respectively, in Fig. 1b, are apparent. These cells mark the large-scale signature of Langmuir turbulence, although in this particular case the system is additionally subjected to bottom-bed influences. The lowest panel in Fig. 1b shows the accompanying instantaneous bed stress, which displays striking spatial



correlation with the above flow structure: the hydrodynamic stresses are largest and smallest beneath zones of predominant downwelling and upwelling, respectively. The spatial distributions of benthic stresses can most readily be understood via consideration of vertical gradients of streamwise velocity, which are necessarily greater beneath downwelling zones; in contrast, upwelling must relax the imposed stresses by virtue of mass conservation arguments. These results provide evidence of a phase-locked modulation between coastal Langmuir turbulence and the hydrodynamic stresses.

In order to further highlight the existence of a flow-stress phase-locked modulation, Fig. 1c, d present time-series visualization of  $\tau_{xz,w}^w(\mathbf{x}_A, t)/u_*^2$  and  $\tilde{w}(\mathbf{x}_B, t)/u_*$ , where the discrete sampling locations are shown on Fig. 1a and summarized in the accompanying caption. The time-series visualizations provide further evidence of phase-locked modulation, wherein the bed stresses rise (i.e., become “more negative”) during times of downwelling. Note that the choice of sampling location,  $\mathbf{x}_A$  and  $\mathbf{x}_B$ , does not effect the resultant deductions: in results not shown here, for brevity, we confirm comparable patterns of correlation where  $\mathbf{x}_B$  is located higher or lower in the column. This result is, by itself, confirmed by inspection of Fig. 1b, which demonstrates that the large-scale Langmuir cell structure is effectively depth-invariant. In addition to the mass conservation arguments already provided on justification for the modulation of bathymetric stress by Langmuir cell pattern, the time-series figures provide further insight on the intensity of mixing within Langmuir cells. It is apparent from inspection of Fig. 1c, d that the signal variability—here illustrated via superposition of upper and lower envelopes, although other metrics such as root-mean-square computed over duration,  $\delta_t U_0/H \approx 400$ , would suffice—is relatively higher and larger within zones of downwelling and upwelling, respectively. The aforementioned ‘shear-normalized’ time is based upon the average sea-surface velocity,  $U_0 = \langle \tilde{u}(x, y, z = H, t) \rangle_{xy}$ . Thus, turbulent kinetic energy,  $k = (1/2)\mathbf{u}' \cdot \mathbf{u}'$ , is higher within downwelling zones, and this high- $k$  fluid impinges on the lower wall, enhancing not only locally-averaged (in time) stress, but also fluctuation magnitudes.

### 3.2 Conditionally-sampled turbulence statistics

In the preceding section, preliminary evidence of a phase-locked flow-stress modulation was provided. In order to fully establish the existence of a modulation, more comprehensive processing of the turbulence statistics is required. One such technique is conditional sampling, which is especially helpful for illumination of flow structures associated with local (space or time) events that are statistically infrequent but dynamically significant [44, 45]. To begin this process, we have generated probability density functions (pdf) of  $\tilde{w}(\mathbf{x}_B, t)/u_*$  and  $\tau_{xz,w}^w(\mathbf{x}_A, t)/u_*^2$ , which are shown in Fig. 2a, b, respectively. Here,  $p(\tilde{w}(\mathbf{x}_B, t)/u_*)$  for coastal Langmuir turbulence exhibits a bimodal pdf, which is the signature of persistent Langmuir circulations (recall Fig. 1d, which showed abrupt transitions between long periods of predominant upwelling and downwelling). For perspective,  $p(\tilde{w}(\mathbf{x}_B, t)/u_*)$  for a canonical turbulent Couette flow is included, too, which lacks the bimodal distribution, owing to the absence of a vortex force.  $p(\tau_{xz,w}^w(\mathbf{x}_A, t)/u_*^2)$  (Fig. 2b) is negatively skewed towards low-frequency, high-magnitude events, further highlighting the importance of associating coastal Langmuir turbulence processes with bathymetric stress.

Figure 2a shows two thresholds— $\tilde{w}(\mathbf{x}_B, t)/u_* = \alpha = -7$  (downwelling) and  $\beta = 4.3$  (upwelling)—which were selected to correspond with an  $\approx 5\%$  probability of occurrence. These thresholds are considered optimal in reconciling the competing goals of recovering spatial attributes of low-frequency flow processes, without excessively-long simulations.



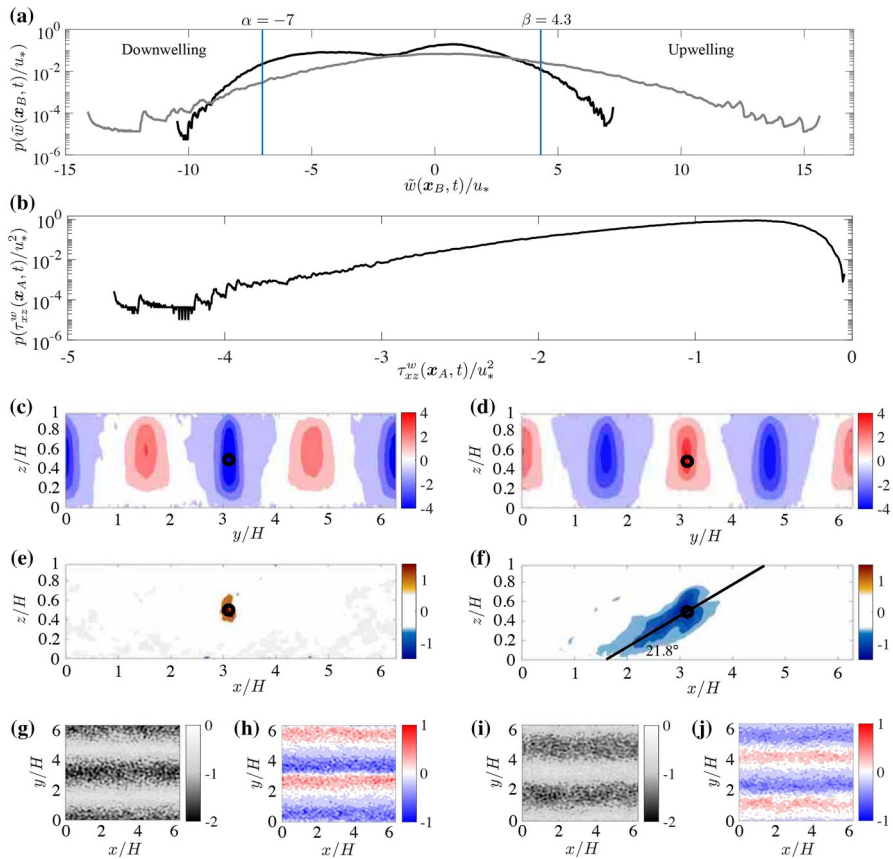


**Fig. 2** Statistical attributes of vertical velocity and bathymetric stress, and flow attributes during periods of predominant downwelling and upwelling: Panel **a** shows a probability density function (pdf) of  $\hat{w}(\mathbf{x}_B, t)$  from a simulation of coastal Langmuir turbulence (solid black) and, for reference, a canonical turbulent Couette flow (solid gray); Panel **b** shows the corresponding pdf of  $\tau_{xz}^w(\mathbf{x}_A, t)$  from simulation of coastal Langmuir turbulence. Panel **a** includes annotation for conditional sampling thresholds,  $\alpha$  and  $\beta$ . Panels **c**, **e**, **g**, **h** and Panels **d**, **f**, **i**, **j** show results from conditional sampling of the flow based on  $\hat{w}(\mathbf{x}_B, t) \leq \alpha$  and  $\hat{w}(\mathbf{x}_B, t) \geq \beta$  (see also Eqs. 4 and 5, and accompanying text). Panels **c**, **d** show  $\hat{w}(\mathbf{x})$  in the  $y$ - $z$  plane; Panels **e**, **f** show  $\hat{u}(\mathbf{x})$  in the  $x$ - $z$  plane; Panels **g**, **i** and Panels **h**, **j** show  $\hat{w}_{xz,w}^w$  and  $\hat{w}_{yz,w}^w$ , respectively, in the  $x$ - $y$  plane. On Panels **c**-**f**, sampling location,  $\mathbf{x}_B$ , is shown for perspective; on Panels **e**, **f**, annotation for the structural inclination has been superimposed

Nevertheless, provided  $\alpha$  and  $\beta$  both correspond with downwelling and upwelling, respectively, the resultant flow patterns will be similar. The choice of threshold does not conceptually alter the scientific deductions attained herein: Langmuir turbulence induces phase-locked modulation of the bathymetric stresses. It is noted that Langmuir cells move laterally in both directions and thus the sampling point,  $\mathbf{x}_B$ , experiences instances of downwelling and upwelling motions. Having nominated the thresholds, conditionally-sampled flow and bathymetric stress can be attained with, respectively:



$$\frac{\hat{u}_\alpha(\mathbf{x})}{u_*} = \left\langle \frac{\tilde{u}(\mathbf{x}, t)}{u_*} \middle| \frac{\tilde{w}(\mathbf{x}_B, t)}{u_*} \leq \alpha \right\rangle_{N_\alpha}, \text{ and } \frac{\hat{u}_\beta(\mathbf{x})}{u_*} = \left\langle \frac{\tilde{u}(\mathbf{x}, t)}{u_*} \middle| \frac{\tilde{w}(\mathbf{x}_B, t)}{u_*} \geq \beta \right\rangle_{N_\beta}, \quad (4)$$

and,

$$\begin{aligned} \frac{\hat{\tau}_{\alpha, iz, w}^w(x, y)}{u_*^2} &= \left\langle \frac{\tau_{iz, w}^w(x, y, t)}{u_*^2} \middle| \frac{\tilde{w}(\mathbf{x}_B, t)}{u_*} \leq \alpha \right\rangle_{N_\alpha}, \text{ and } \frac{\hat{\tau}_{\beta, iz, w}^w(x, y)}{u_*^2} \\ &= \left\langle \frac{\tau_{iz, w}^w(x, y, t)}{u_*^2} \middle| \frac{\tilde{w}(\mathbf{x}_B, t)}{u_*} \geq \beta \right\rangle_{N_\beta}, \end{aligned} \quad (5)$$

where  $N_\alpha$  and  $N_\beta$  are the number of instances of threshold exceedance, and  $\langle \cdot \rangle_{N_\alpha}$  and  $\langle \cdot \rangle_{N_\beta}$  denote averaging over  $N_\alpha$  and  $N_\beta$  instances, respectively; in Eq. 5, subscript  $i = x$  and  $y$  (i.e., streamwise-vertical and spanwise-vertical shear stresses, respectively).

Figure 2c, d show conditionally-averaged vertical velocity based upon  $\tilde{w}(\mathbf{x}_B, t)/u_* \leq \alpha$  and  $\tilde{w}(\mathbf{x}_B, t)/u_* \geq \beta$ , respectively. The sampling location has been superimposed on the panels, for perspective. The sampling point is enveloped within a zone of coherent downwelling and upwelling, respectively, when sampled for  $\tilde{w}(\mathbf{x}_B, t)/u_* \leq \alpha$  and  $\tilde{w}(\mathbf{x}_B, t)/u_* \geq \beta$ , respectively; in both cases, the prominent downwelling(upwelling) zone is flanked laterally by adjacent zones of upwelling (downwelling). These figures provide clear evidence of a spanwise pattern of Langmuir cells, where the zone of downwelling occupies the depth of the column while the upwelling zone is relatively smaller. This provides additional evidence that downwelling induces a greater modulation of the hydrodynamic bathymetric stress. Figure 2e, f show  $\hat{u}'_\alpha$  and  $\hat{u}'_\beta$ , but in the  $x$ - $z$   $x$ - $z$  plane. This figure is helpful for recovering the streamwise nature of Langmuir cells. Within the downwelling zone (Panel e), there is a region of relative streamwise momentum excess proximal to the sampling point, beyond which  $\hat{u}'_\alpha \approx 0$ ; thus, the downwelling zones exhibit virtually no streamwise dependence. Within the upwelling zones, however, the picture is entirely different, wherein we recover evidence of an inclined plume of relative momentum deficit. The inclination angle,  $\gamma = 21^\circ$ , has been superimposed, as this value is  $\approx 25\%$  larger than the inclination angle reported for large-scale motions in canonical wall-sheared flows [46]. Although outside the scope of this article, the result suggests that within upwelling zones the flow is dynamically similar to such canonical wall flows. The result also suggests that the tube-like structure of Langmuir cells is, in fact, only strictly applicable to the downwelling zones; within upwelling zones, it is statistically possible for streamwise-heterogeneous structures or tube-like upwelling zones to exist. Finally, we emphasize that Fig. 1b–d served as preliminary evidence that within downwelling(upwelling) zones, bathymetric stress is relatively stronger(weaker). The contour for  $\hat{u}'_\beta$  confirms, indeed, that the zone of relative momentum deficit extends to regions immediately above the seafloor, which guarantees a relatively-lower bathymetric stress.

Figures 2g, h and 2i, j show spatial distributions of  $\hat{\tau}_{\alpha, iz, w}^w$  and  $\hat{\tau}_{\beta, iz, w}^w$ , respectively. These figures provide definitive evidence that bathymetric stress is subjected to a phase-locked modulation by the large-scale attributes of Langmuir cells. Beneath downwelling zones (Panels g, h),  $\hat{\tau}_{\alpha, iz, w}^w$  exhibits a strip of elevated stress beneath the sampling location,  $y/H = 3$ , which is flanked laterally by relatively lower stress. This result is entirely consistent with Panel (c), which shows coherent downwelling over the depth of the column. By virtue of mass conservation, downwelling fluid induces a lateral outflow at the seafloor, which induces a spanwise vertical velocity that manifests itself in the



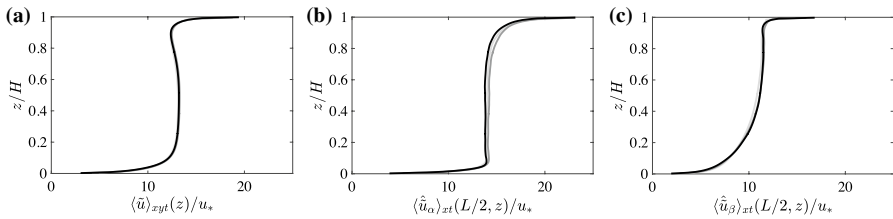


**Fig. 3** Vertical profiles of Reynolds- and conditionally-averaged streamwise velocity: **a**  $\langle \tilde{u} \rangle_{xyt}(z)/u_*$ ; **b**  $\langle \hat{u}_\alpha \rangle_{xt}(L/2, z)/u_*$ ; and **c**  $\langle \hat{u}_\beta \rangle_{xt}(L/2, z)/u_*$ . On each panel, solid black, gray, and light gray profiles correspond with results from LES with  $\{N_x, N_y, N_z\} = \{192, 192, 192\}$ ,  $\{128, 128, 128\}$ , and  $\{96, 96, 96\}$ , respectively

$\hat{\tau}_{\alpha, yz, w}^w$  pattern (Panel h). Equivalent colorbar limits were deliberately imposed on Panels (g, i) and Panels (h, j), in order to contrast the different stress patterns due to upwelling and downwelling. Clearly, beneath an upwelling zone,  $\hat{\tau}_{\beta, xz, w}^w$  does attain values of the magnitude exhibited by  $\hat{\tau}_{\alpha, xz, w}^w$ . Moreover, beneath the sampling location,  $y/H = 3$ , we see a strip of relatively low stress, which is consistent with Fig. 1. The spatial distribution of  $\hat{\tau}_{\beta, yz, w}^w$  is effectively a reverse of the  $\hat{\tau}_{\alpha, yz, w}^w$  distribution—since in the case of upwelling a lateral inflow occurs at the seafloor. Again, it is apparent by inspection that  $\hat{\tau}_{\alpha, yz, w}^w$  attains values larger than  $\hat{\tau}_{\beta, yz, w}^w$ .

As a final, closing result, we have prepared vertical profiles of streamwise velocity following several averaging operations, which are shown in Fig. 3. Panel (a) shows the Reynolds-averaged profile, while Panels (b) and (c) show  $\langle \hat{u}_\alpha \rangle_{xt}(L/2, z)/u_*$  and  $\langle \hat{u}_\beta \rangle_{xt}(L/2, z)/u_*$ , respectively. On each panel, we show results from the three resolutions considered for this study. The results clearly demonstrate—at least to first order—that the LES predictions are resolution invariant. Moreover, we note that the profiles are similar to those reported from LES modeling of a similar flow [15], thus further demonstrating efficacy of the LES predictions. The Reynolds-averaged profile is intermediate to the profile associated with downwelling (Panel b) and upwelling (Panel c). Importantly, it is apparent from inspection that  $\partial_z \langle \hat{u}_\alpha \rangle_{xt}(L/2, z)/u_* > \partial_z \langle \hat{u}_\beta \rangle_{xt}(L/2, z)/u_*$ : surface shear, which sustains bathymetric stress, is relatively stronger beneath downwelling zones. This is thoroughly consistent with comments made in relation to Fig. 1, and throughout this manuscript.

## 4 Concluding remarks

Numerical solutions of the wave-averaged Craik–Leibovich equations, applied with initial and boundary conditions representing natural coastal zones, yield coherent, full-depth, counter-rotating Langmuir cells. We find that these cells extend to the depth of the water column, thus affecting the bottom-boundary layer dynamics and bathymetric stress. Through a series of developments and via flow processing techniques, we have been able to demonstrate phase-locked modulation of bathymetric stress by coastal Langmuir turbulence. This novel result demonstrates that Langmuir turbulence—an ocean boundary layer state realized under favorable wind- and wave-forcing conditions—has special implications for coastal turbidity and benthic sequestration of suspended quantities, among other problems of practical relevance.



**Acknowledgements** This research was supported by the Texas General Land Office, Oil Spill Program (Program Manager: Steve Buschang) under TGLO Contract # 18-130-000-A670. Computational resources were provided by Texas Advanced Computing Center at The University of Texas at Austin.

## Compliance with ethical standards

**Conflict of interest** The authors declare that they have no conflict of interest.

## References

1. Lehr W, Beatty D (2000) The relation of Langmuir circulation processes to the standard oil spill spreading, dispersion and transport algorithms. *Spill Sci Technol Bull* 6:247
2. Thorpe S (2000) Langmuir circulation and the dispersion of oil spills in shallow seas. *Spill Sci Technol Bull* 6:213
3. McWilliams J, Sullivan P (2000) Vertical mixing by Langmuir circulations. *Spill Sci Technol Bull* 6:225
4. Dyke P, Barstow S (1983) The importance of Langmuir circulations to the ecology of the mixed layer in North sea dynamics. Springer, Berlin: Sundermann/Lenz, pp 486–497
5. Denman K, Gargett A (1995) Biological physical interactions in the upper ocean—the role of vertical and small-scale transport processes. *Annu Rev Fluid Mech* 27:225
6. Belcher S, Grant A, Hanley K, Fox-Kemper B, Roedel L, Sullivan P, Large W, Brown A, Hines A, Calvert D, Rutgersson A, Pettersson H, Bidlot JR, Janssen P, Polton J (2012) A global perspective on Langmuir turbulence in the ocean surface boundary layer. *Geophys Res Lett* 39:L18605
7. Craik A, Leibovich S (1976) A rational model for Langmuir circulation. *J Fluid Mech* 73:401
8. Craik A (1977) The generation of Langmuir circulations by an instability mechanism. *J Fluid Mech* 81:209
9. Leibovich S (1977) Convective instability of stably stratified water in the ocean. *J Fluid Mech* 82:561
10. Langmuir I (1938) Surface motion of water induced by wind. *Science* 87:119
11. McWilliams J, Sullivan P, Moeng C (1997) Langmuir turbulence in the ocean. *J Fluid Mech* 334:1
12. Yang D, Chamecki M, Meneveau C (2014) Inhibition of oil plume dilution in Langmuir ocean circulation. *Geophys Res Lett* 41:1632
13. Gargett A, Wells J, Tejada-Martínez A, Grosch C (2004) Langmuir supercells: a mechanism for sediment resuspension and transport in shallow seas. *Science* 306:1925
14. Gargett A, Wells J (2007) Langmuir turbulence in shallow water. Part 1. Observations. *J Fluid Mech* 576:27
15. Tejada-Martínez A, Grosch C (2007) Langmuir turbulence in shallow water. Part 2. Large-eddy simulation. *J Fluid Mech* 576:63
16. Tejada-Martínez A, Grosch C, Sinha N, Akan C, Martinat G (2012) Disruption of bottom log-layer in LES of full-depth Langmuir circulation. *J Fluid Mech* 699:79
17. Shrestha K, Anderson W, Kuehl J (2018) Langmuir turbulence in coastal zones: structure and length scales. *J Phys Oceanogr* 48:1089
18. Deng B, Yang Z, Xuan A, Shen L (2019) Influence of Langmuir circulations on turbulence in the bottom boundary layer of shallow water. *J Fluid Mech* 861:275
19. Shrestha K, Anderson W, Tejada-Martínez A, Kuehl J (2019) Orientation of coastal-zone Langmuir cells forced by wind, wave and mean current at variable obliquity. *J Fluid Mech* 879:716
20. Kukulka T, Pleuddemann A, Sullivan P (2012) Nonlocal transport due to Langmuir circulation in a coastal ocean. *J Geophys Res* 117:C12007
21. Sinha N, Tejada-Martínez A, Akan C (2015) Toward a K-profile parameterization of Langmuir turbulence in shallow coastal shelves. *J Phys Oceanogr* 45:2869
22. Walker R, Tejada-Martínez A, Chester E (2016) Large-Eddy Simulation of a coastal ocean under the combined effects of surface heat fluxes and full-depth Langmuir circulation. *J Phys Oceanogr* 46:2411
23. Savidge D, Gargett A (2017) Langmuir supercells on the middle shelf of the South Atlantic Bight: 1. Cell structure. *J Mar Res* 75:49
24. Golshan R, Tejada-Martínez A, Juha M, Bazilevs Y (2017) LES and RANS simulation of wind- and wave-forced oceanic turbulent boundary layers in shallow water with wall modeling. *Comput Fluids* 142:96



25. Zedel L, Farmer D (1991) Organised structures in subsurface bubble cloud: Langmuir circulation in the open ocean. *J Geophys Res* 96:8889
26. Smith J (1998) Evolution of Langmuir circulation during a storm. *J Geophys Res Oceans* 103:12649
27. Thorpe S (2004) Langmuir circulation. *Annu Rev Fluid Mech* 36:55
28. Tejada-Martínez A, Akan C, Grosch NSC, Martinat G (2013) Surface dynamics in LES of full-depth Langmuir circulation in shallow water. *Phys Scr T155:014008*
29. Orlu R, Schlatter P (2011) On the fluctuating wall-shear stress in zero pressure-gradient turbulent boundary layer flows. *Phys Fluids* 23:021704
30. Jacob C, Anderson W (2016) Conditionally averaged large-scale motions in the neutral atmospheric boundary layer: insights for aeolian processes. *Boundary-Layer Meteorol*. <https://doi.org/10.1007/s10546-016-0183-4>
31. Smith WN, Katz J, Osborn T (2005) On the structure of turbulence in the bottom boundary layer of the coastal ocean. *J Phys Oceanogr* 35:72
32. Martinat G, Xu Y, Grosch C, Tejada-Martínez A (2011) LES of turbulent surface shear stress and pressure-gradient-driven flow on shallow continental shelves. *Ocean Dyn* 61:1369
33. Gargett A, Grosch C (2014) Turbulence process domination under the combined forcings of wind stress, the Langmuir vortex force, and surface cooling. *J Phys Oceanogr* 44:44
34. Akan C, Tejada-Martínez AE, Grosch C, Martinat G (2013) Scalar transport in large-eddy simulation of Langmuir turbulence in shallow water. *Cont Shelf Res* 55:1
35. Pope S (2000) *Turbulent flows*. Cambridge University Press, Cambridge
36. Bou-Zeid E, Meneveau C, Parlange M (2005) A scale-dependent Lagrangian dynamic model for large eddy simulation of complex turbulent flows. *Phys Fluids* 17:025105
37. Willingham D, Anderson W, Christensen KT (2013) Turbulent boundary layer flow over transverse aerodynamic roughness transitions: induced mixing and flow characterization. *J Barros Phys Fluids* 26:025111
38. Anderson W, Barros J, Christensen K, Awasthi A (2015) Numerical and experimental study of mechanisms responsible for turbulent secondary flows in boundary layer flows over spanwise heterogeneous roughness. *J Fluid Mech* 768:316
39. Anderson W (2019) Non-periodic phase-space trajectories of roughness-driven secondary flows in high- $Re_\tau$  boundary layers and channels. *J Fluid Mech* 869:27
40. Deigaard R, Fredsoe J (1989) Shear stress distribution in dissipative water waves. *Coast Eng* 13:357
41. Arnskov M, Fredsoe J, Sumer B (1993) Bed shear stress measurements over a smooth bed in three-dimensional wave-current motion. *Coast Eng* 20:277
42. Orszag S (1970) Transform method for calculation of vector coupled sums: application to the spectral form of the vorticity equation. *J Atmos Sci* 27:890
43. Albertson J, Parlange M (1999) Surface length scales and shear stress: implications for land-atmosphere interaction over complex terrain. *Water Resour Res* 35:2121
44. Antonia R (1981) Conditional sampling in turbulence measurement. *Annu Rev Fluid Mech* 13:131
45. Adrian R (1988) Linking correlations and structure: stochastic estimation and conditional averaging. In: Zoran P (ed) *Zaric memorial international seminar on near-wall turbulence*. Hemisphere
46. Hutchins N, Marusic I (2007) Evidence of very long meandering features in the logarithmic region of turbulent boundary layers. *J Fluid Mech* 579:1

**Publisher's Note** Springer Nature remains neutral with regard to jurisdictional claims in published maps and institutional affiliations.